Army Research Laboratory

Light Scattering from Deformed Droplets and Droplets with Inclusions:

Volume I. Experimental Results

David R. Secker, Richard Greenaway, Paul H. Kaye, Edwin Hirst,
David Bartley, and Gorden Videen

DTIC QUALITY INSPECTED 4

20001106 004

Army Research Laboratory

Adelphi, MD 20783-1197

Light Scattering from Deformed Droplets and Droplets with Inclusions:

Volume I. Experimental Results

David R. Secker, Richard Greenaway, Paul H. Kaye, Edwin Hirst
University of Hertfordshire, Hatfield, UK

David Bartley
National Institute for Occupational Safety and Health, Cincinnati, OH

Gorden Videen
Computational and Information Sciences Directorate, ARL

Abstract

This is the first of two volumes dealing with experimental and theoretical results from the scattering of light by deformed liquid droplets and droplets with inclusions. Characterizing droplet deformation could lead to improved measurement of droplet size by commercial aerodynamic particle sizing instruments. Characterizing droplets with inclusions can be important in some industrial, occupational, and military monitoring scenarios. The nozzle assembly from a TSI aerodynamic particle sizer was used to provide the accelerating flow conditions in which experimental data were recorded. A helium-neon (HeNe) laser was employed to generate the light-scattering data, and an externally triggered, pulsed copper vapor laser provided illumination for a droplet imaging system, arranged orthogonal to the HeNe scattering axis. The observed droplet deformation correlates well over a limited acceleration range, with theoretical predictions derived from analytical solution of the Navier-Stokes equation.

Contents

Figures

1. Introduction

The authors are currently investigating light-scattering methods that could be used to correct for the errors that are known to occur in the measurement of liquid droplets by commercial aerodynamic particle sizing instruments. In the course of the investigation, it became apparent that the apparatus used for droplet deformation studies was also capable of reproducibly generating droplets with inclusions. These droplets with inclusions are important because they can be representative of aerosols found in hospital or battlefield environments, where biological organisms can survive for prolonged periods when contained within a protective liquid coating. This volume therefore describes the acquisition of experimental light-scattering data from both deformed droplets and droplets with inclusions. These data may be used to help develop and test theoretical inversion algorithms, some of which are described in volume 2, which could ultimately allow rapid characterization and/or identification of these droplet morphologies. This, in turn, could lead to improvements in commercial aerodynamic particle sizers and new opportunities for the development of light-scattering aerosol monitoring instruments for bioaerosol detection.

1.1 Aerodynamic Particle Sizers

The size of an airborne droplet may be defined in a number of ways, depending on the method of measurement. However, in studies of therapeutic aerosol sprays, combustion aerosols, paint sprays, and coatings, where on-line or real-time measurements are required and/or where the airborne behavior of the droplet is relevant to the application, the aerodynamic size d_a is frequently sought. The parameter d_a is defined as the diameter of a unit density sphere with the same gravitational settling velocity as the particle in question. The traditional method of determining the aerodynamic size of a particle was to measure its gravitational settling velocity with suitable sedimentation instruments. This process was slow and laborious, and commercial instruments based on the acceleration of particles were developed as an alternative [1]. The most widely used commercial aerodynamic sizers are the TSI aerodynamic particle sizer (APS) family of instruments (APS 3300 series, TSI, Inc., St Paul, MN), which measure the particle size by accelerating a sample airstream in which the particles are suspended and measuring the velocity acquired by individual particles. The larger particles exhibit greater inertia and thus accelerate more slowly, thereby attaining lower velocities. In the TSI APS instruments, an aerodynamic accelerating nozzle, in which a sample flow is sheathed in filtered air, produces the necessary accelerating flow, as illustrated in figure 1. The total airflow through the nozzle is regulated to 5 l/min, 4 l/min of which is filtered to provide the sheath flow. The time of flight of the particle through two closely spaced

1

Figure 1. Schematic
diagram of particle
delivery system used
in TSI APS 3300 series
instruments.
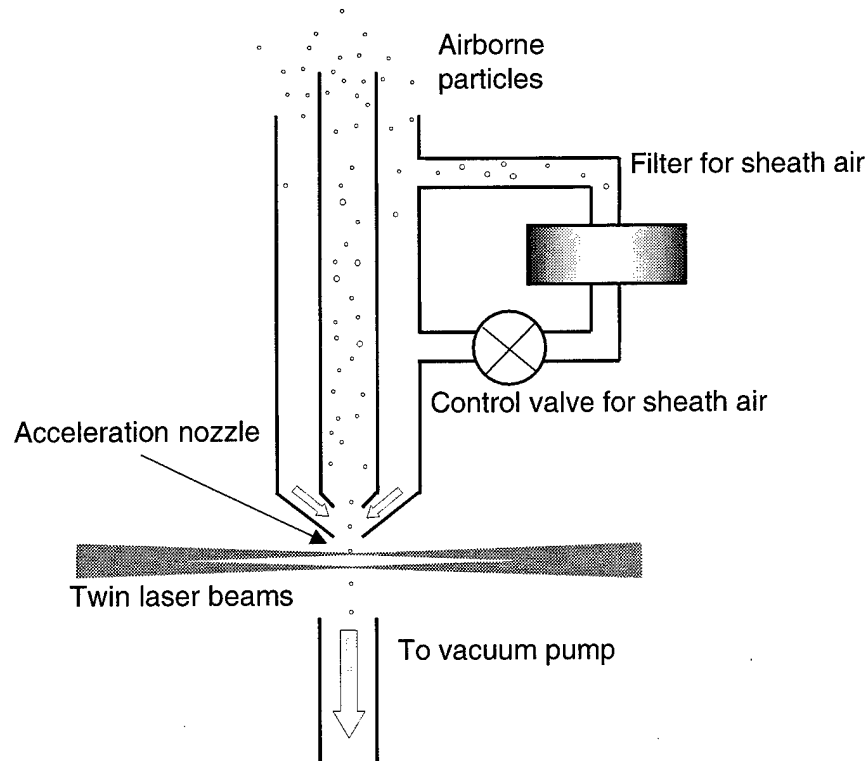
laser beams positioned a few hundred micrometers beneath the nozzle exit
is recorded from the pulses of light scattered by the particle to an optical
detector. The particle's aerodynamic size is assessed by relating the transit
time to an internal calibration function based on measured times of flight of
solid spherical calibration particles. The size range covered by this instru-
ment is from 0.5 to 30 μm aerodynamic diameter, depending on the instru-
ment model used.

However, aerodynamic sizing instruments of this type suffer a significant
limitation in that the measured aerodynamic size can be significantly af-
fected by particle shape. When one attempts to measure nonspherical par-
ticles of known density, the shape (and orientation) of each particle sub-
jected to the accelerating air flow governs the drag force it experiences and
hence affects the measured aerodynamic size. The measurement of liquid
aerosol droplets is subject to significant error (25% undersizing reported in
some cases) because the droplets deform to oblate spheroids in the acceler-
ating airflow. As a result of this deformation, their cross-sectional area in-
creases, and they experience a greater acceleration than would be the case
with similar-sized rigid spheres. Despite this phenomenon being well re-
ported in the past by Baron [2] and Griffiths et al [3], there is as yet no
systematic method of measuring the degree of deformation experienced by
individual droplets in the instrument- and material-specific calibration
curves, derived, for example, through gravitational settling techniques.

2

1.2 Spatial Light Scattering

The spatial distribution of light scattered by a particle, also referred to in certain texts as the two-dimensional angular optical scattering (TAOS) pattern [4], is a complex function of the size, shape, dielectric structure, and orientation of the particle, as well as of the properties of the illuminating radiation (wavelengths, polarization state). Analysis of the scattering pattern can provide a means of characterizing the shape, orientation, and internal structure of the illuminated particle, and many researchers have exploited this property in various ways. Previous work by the authors [5] has explored the potential of scattering pattern analysis for particle shape and size classification and has demonstrated [6,7] how such techniques may be implemented in real-time airborne particle measurement systems designed for ambient aerosol characterization and asbestos fiber detection.

Scattering patterns can cover different scattering angle ranges, depending on the light-collection geometry used to acquire them. The examples shown in figure 2 (see figure caption for description of particle types) were recorded by the imaging of the pattern of light scattered by individual particles onto an intensified charge-coupled device (ICCD) camera as the particles were carried by an airstream through a laser beam. The particle transition time through the beam was ~2 μs, and in each case light scattered between 5° and 30° scattering angles and throughout 360° of azimuth was captured as a 256 × 256 pixel image. The beam direction is perpendicular to the paper into the center of each image. Each white dot in the patterns corresponds to a single scattered photon, and the images thus represent photon distribution maps of several thousands to several tens of thousands of scattered photons. The images illustrate the wide variations of different particle shapes and orientations that these patterns can assume. It was the potential of spatial light-scattering analysis for real-time particle shape characterization that initiated the fundamental study of droplet scattering reported here. It also underpins an ultimate aim of this work—to provide an on-line optical means of correcting for the errors in measured aerodynamic size caused by droplet deformation in instruments such as those in the APS 3300 series.

Figure 2. Examples of spatial light scattering patterns from individual airborne particles: (a) hematite ellipsoid, 2 µm; (b) copper flake, ~5 µm; (c) sodium chloride crystal; (d) sodium chloride crystal; (e) asbestos fiber (crocidolite); (f) irregular background particle; (g) asbestos fiber (chrysotile); and (h) water droplet, ~9 µm diameter.
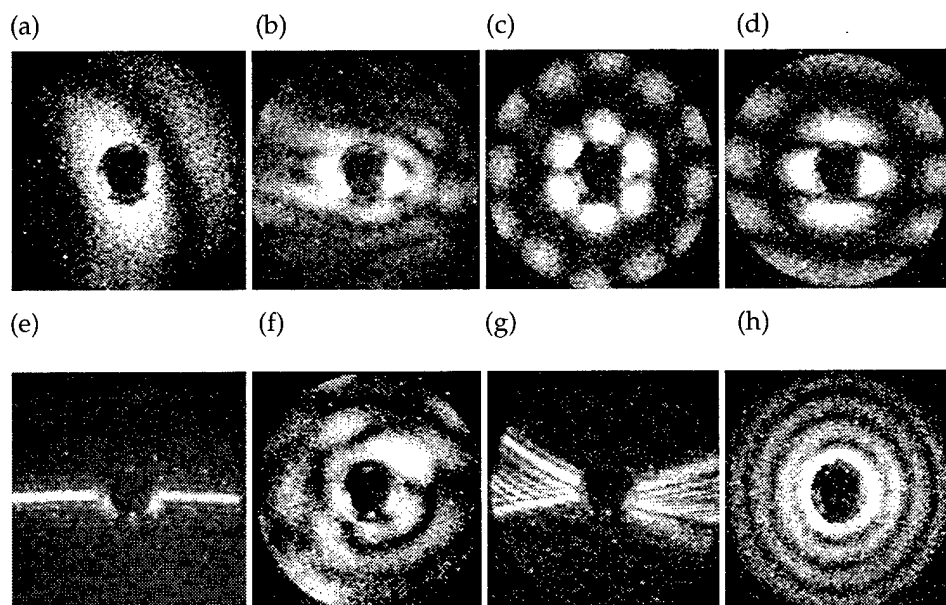
2. Apparatus

An apparatus was constructed that allowed the acquisition of both spatial scattering patterns and real images from individual droplets in the sub-30-μm size range as they traversed the measurement space below an APS 3320 sample delivery nozzle (donated by TSI, Inc.). The apparatus is shown schematically in figure 3. As stated earlier, the actual TSI APS 3300 series of instruments incorporates two closely spaced cross-polarized beams and measures particle time-of-flight between the beams. However, for the fundamental results reported here, the spatial light-scattering pattern images were produced with a single beam from a 633-nm, 15-mW plane polarized helium-neon (HeNe) laser (model 05-LHP-151, Melles Griot, Inc., Carlsbad, CA). Furthermore, while the normal operating flow rate of the TSI APS instrument is 5 l/min (1 l/min of sample flow rate and 4 l/min of filtered sheath flow), we have additionally observed droplet behavior over a range of flow conditions, both less than and greater than the norm, to gain a greater understanding of the morphological changes taking place.

Figure 3. Schematic diagram of apparatus used to acquire scattering patterns and real images from individual airborne droplets.

5
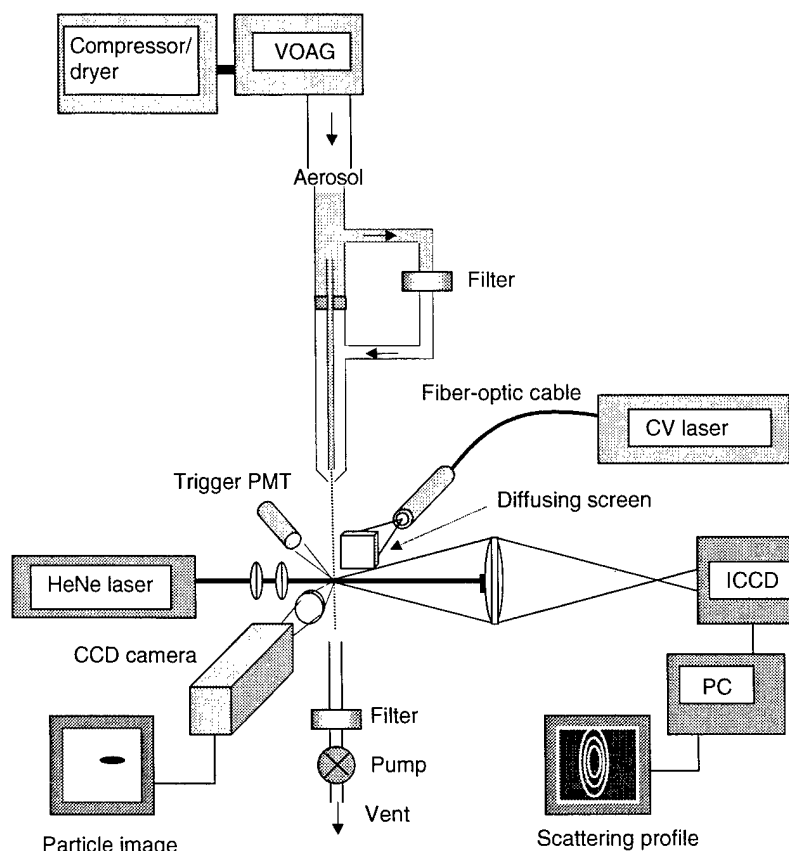
2.1 Light-Scattering Pattern Acquisition

The beam from the HeNe laser passes through a quarter-wave plate to render the light circularly polarized before it is focused through a cylindrical lens to produce a beam of elliptical cross section (approximately 1.2 mm by 100 μm) at the point of intersection with the sample air flow. Monodisperse droplets are generated into the sample flow by a vibrating orifice aerosol generator (VOAG) (manufactured by TSI, Inc.), as described next. As each droplet traverses the beam, light scattered in the forward direction between angles of 5° and 20° is imaged onto an intensified, asynchronously triggered ICCD camera (ICCD225, Photek Ltd., East Sussex, UK). The lower angular limit is set by a beam stop, while the higher limit is set to avoid shadowing of the scattered light by the lower surface of the sample delivery nozzle. Images from the camera are digitized, displayed, and stored on a computer at a rate of several images per second for later analysis. A trigger signal for the acquisition of a scattering pattern by the camera is derived from a separate photomultiplier detector module, which receives light scattered at a higher scattering angle than the camera, as indicated in figure 3. The rising and trailing edges of the signal from the photomultiplier detector respectively initiate and terminate the camera integration period, which is typically ~2 μs duration.

2.2 Droplet Image Acquisition

Real images of the droplets are acquired with a charge-coupled device (CCD) camera assembly, mounted orthogonal to the HeNe scattering axis. In the manner first described by Baron [3,8], the droplets are viewed against a bright diffusing screen. The illumination for this screen is derived from a copper vapor laser (Oxford Lasers Ltd., UK) that delivers 38-ns pulses at wavelengths of 510 and 578 nm. Each pulse has an energy of approximately 2 mJ. Again, appropriate triggering of the laser pulses is achieved by use of the signal from the photomultiplier detector. The imaging system uses a high numerical aperture microscope objective lens and a standard microscope tube, resulting in an overall image magnification of approximately 10×. A digital, nonintensified CCD camera (model KP-F100, Hitachi Denshi Ltd., Tokyo, Japan) was used to acquire images, because it offered both high read-out speed and small pixel size (6.7 μm²). This pixel size produced images of acceptable resolution, the diameter of a 20-μm droplet, for example, covering approximately 30 pixels within a 1300 × 1030 pixel image. A Foucault knife-edge test [9] was performed to determine the resolution of three pixels for the image quality attainable with this configuration.

We originally intended to acquire scattering patterns and real images simultaneously from the same droplet. This would have required appropriate optical filtering to prevent the intense illumination from the copper vapor laser from reaching the ICCD camera. However, because the pulsed radiation was broad-field (as a result of the diffusion screen) and multiwavelength, the task of attenuating this radiation to a degree sufficient to

6

prevent damage to the ICCD camera was extremely difficult without also significantly attenuating the 633-nm scatter light flux. Fortuitously, the uniformity of droplet size produced by the VOAG for a given set of generating conditions was such that the scattering patterns and images from successive droplets were remarkably reproducible, the differences being principally a result of the optical quantization noise. We therefore decided to avoid potential overillumination of the ICCD by recording the scattering patterns and real droplet images from successive droplets rather than the same droplet, ensuring that the ICCD was disabled during the firing of the pulsed laser.

2.3 Droplet Generation and Delivery

The VOAG produces droplets by inducing mechanical instability in a fine liquid jet through excitation with a piezoelectric oscillator. When first formed, droplets are comparatively large and compose a solute—in our case, either oleic acid or glycerol—in solution with AR-grade isopropyl alcohol. Dry (<1 %RH) compressed air is used to transport the droplet aerosol from the VOAG drying column to the light-scattering instrument, during which time the alcohol evaporates, to leave pure oleic acid or glycerol droplets. A bleed valve controls the total flow rate through the nozzle subsystem. For the experiments described, the total flow rate was set before the scattering data were acquired, and the sheath air flow rate was measured before and during acquisition with a bubble flowmeter. The measured sample flow rate, consistently 20 percent of the total flow rate, was found to be stable to within 1 percent during the period of experimental data acquisition.

3. Experimental Data

All experimental data presented here were recorded from oleic acid droplets (with the exception of those shown later in fig. 8b, which shows scattering from a glycerin droplet). Figure 4 illustrates the changes that occur in the spatial light-scattering patterns from individual droplets, as a function of both droplet size and increasing sample flow rate. Each scattering pattern was recorded over a 2-μs period as the droplet traversed the HeNe beam beneath the aerosol delivery nozzle. Each scattering pattern therefore represents the forward scattering from a deformed droplet illuminated at 90° to its axis of symmetry. The images on the top row were recorded from 8-μm-diameter droplets at total flow rates from 1 to 6 l/min. Subsequent rows show the scattering behavior of 12-, 16-, 20-, 25-, and 30-μm-diameter droplets for similar values of flow rate. The gain of the image intensifier was reduced for larger droplet sizes (and lower droplet velocities) to minimize optical saturation effects, although these are still visible as extended solid white areas in some of the larger droplet/lower velocity patterns. Ananth and Wilson [10] have carried out a theoretical analysis of the gas

Figure 4. Spatial light-scattering patterns from individual droplets as function of droplet size and sample flow rate.
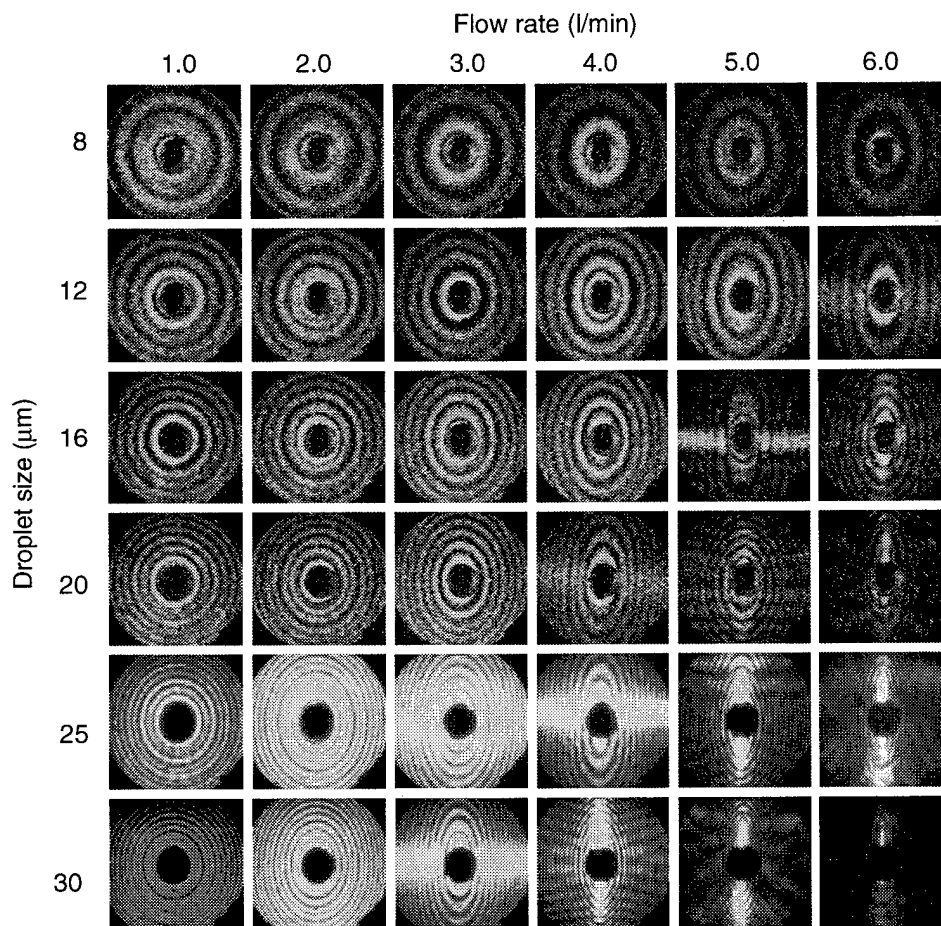
and particle velocities present in the APS delivery nozzle. Their results predict that at the normal APS operational flow rate of 5 l/min, the gas velocity at the measurement point is approximately 160 m/s, and the velocity of a 10-μm spherical particle is approximately 50 m/s.

At the lowest flow rate and smallest droplet size (top left image in fig. 4), the scattering pattern correlates closely with that predicted by the Mie theory [11] for a perfect sphere. No droplet deformation is discernible from the light-scattering data in this image. For increasing flow rate and/or droplet size, however, the degree of droplet deformation would be evident from an increasing ellipticity of the scattering maxima and minima evident on the patterns. This behavior appears well behaved to a point, such as at 16 μm × 5 l/min, when bright horizontal barring occurs on the image. This is predicted by the theoretical analysis described in volume 2 of this report [12]. This barring may occur either as a predominant central white bar or as a series of parallel horizontal scattering fringes, such as those visible at 20 μm × 5 l/min. Increasing the flow rate or droplet size further results in more complex interference patterns within the images, such as those seen at 30 μm × 5 l/min. This behavior appears to indicate that the droplets are undergoing a transition from simple oblate spheroidal form to the more complex morphologies first observed by Baron [2]. It also indicates that the task of attempting to rapidly assess the deformation of a single droplet by analysis of its light-scattering pattern (as we desire for on-line correction of deformation effects in aerodynamic sizing) is nontrivial for droplets deformed beyond a certain degree.

Figure 5 shows light-scattering pattern images for undistorted droplet diameters of 20, 25, and 30 μm, and total flow rates from 1 to 6 l/min. Adjacent to each scattering pattern is the corresponding droplet image. These latter images indicate the changes in droplet shape that produce the increasingly complex scattering data. The essentially perfect spheres undergo flattening into oblate spheroids, and then become biconcave disks before forming menisci with concave upper surfaces. This morphological transition coincides with the dominant feature of the respective scattering patterns, changing from a horizontal to a vertical bright band, the former possibly the result of a morphology-dependent resonance in the droplet, and the latter a function of the increasingly narrow horizontal cross section that the droplet presents. We are currently investigating these effects further, with the hope of elucidating the causes of the dominant scattering features.

Figure 5. Spatial light-scattering patterns and droplet images for 20-, 25-, and 30-µm-diameter droplets at various sample flow rates through APS aerosol delivery nozzle.

Spherical droplet size (µm)

Flow rate (l/min)

Direction of particle motion

10
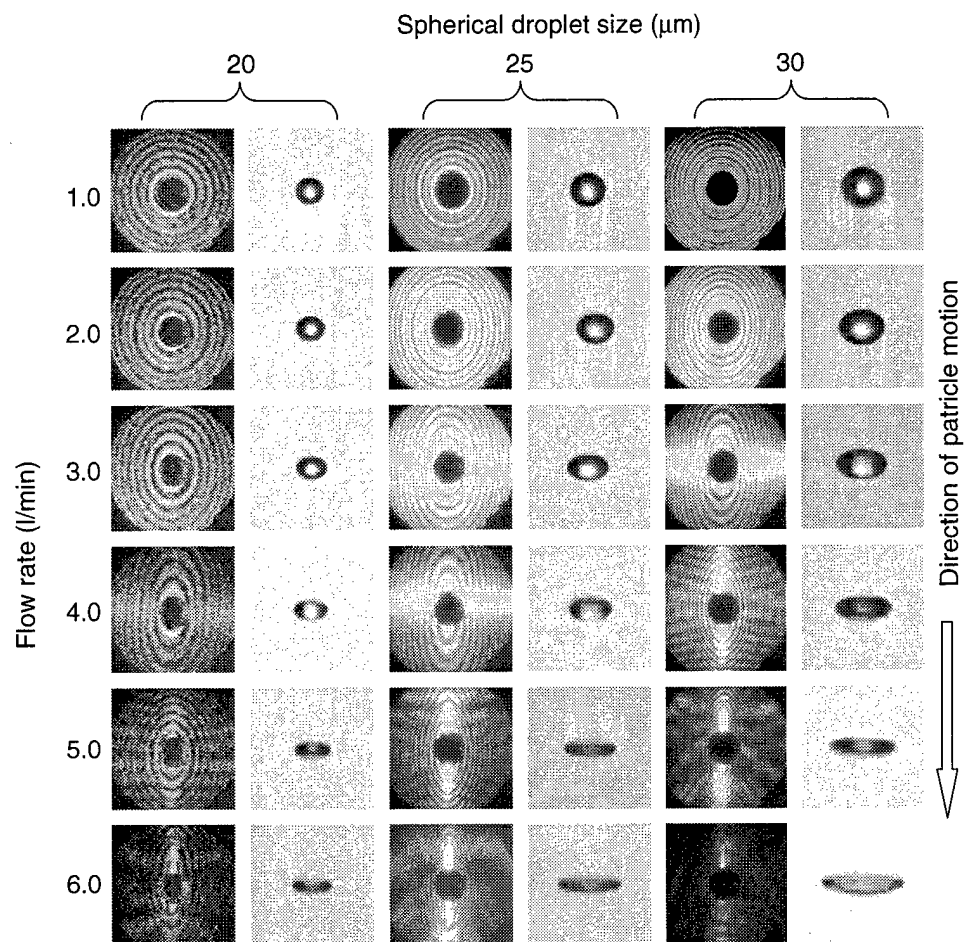
4. Quantifying Droplet Deformation

Inversion of the light-scattering data to yield droplet deformation descriptors is addressed in volume 2 of this report [12]. As a comparative measure, a first-order estimate of droplet deformation under given flow conditions may be obtained from the Feret ratio of the droplet image, defined as the ratio of Feret diameters, i.e., the maximum distances between particle edges in the x and y directions of the image (orthogonal and parallel to the particle trajectory, respectively). The edges of the droplets, $E(x,y)$, were determined by a computer-based Gaussian edge-detection algorithm [13]. The threshold value for this algorithm can be set manually or left to be determined automatically from the background intensity. Since the background intensity is different for each image, we used the automatic threshold function. In addition, the graininess of the background can make the algorithm detect erroneous edges there. However, the algorithm generally provides a continuous line that is evident as an edge in the binary file that the algorithm creates. The Feret ratio can then be determined from this binary file. Figure 6 shows a plot of Feret ratio versus flow rate for 20-µm oleic acid droplets. As can be seen from the figure, the Feret ratio is well behaved up to a 4.5-1/min flow rate. The reduction in the rate of increase of the Feret ratio immediately after this point coincides with the droplet beginning to assume a meniscus form (see fig. 5), for which the Feret ratio is less. The change in the curve at the 4.5-1/min flow rate coincides with the point at which the horizontal banding appears in the scattering pattern. A significant part of the experimental uncertainty in the Feret ratio measurements is caused by a blurring of the droplet images in the direction of motion, especially at higher flow rates. Methods to minimize motion blur by reduction of the laser pulsewidth are currently being explored.

Liquid droplet distortion produced in an accelerating flow field has been computed through analytical solution of the Navier-Stokes equation by Bartley et al [14], and this has led to a means of correlating observed droplet deformation to such parameters as droplet diameter, viscosity, surface tension, and density. A high-Reynolds-number empirical approximation to the pressure external to the droplet has been used in these calculations. This procedure, described in detail by Bartley et al, correctly predicts the change in droplet shape with increasing flow rate from spherical to spheroidal to biconcave disk. For example, figure 7 shows the image of a 20-µm nominal diameter oleic acid droplet, together with the corresponding computed cross section. Beyond this level of distortion, the theoretically computed shape pattern is not reliable.

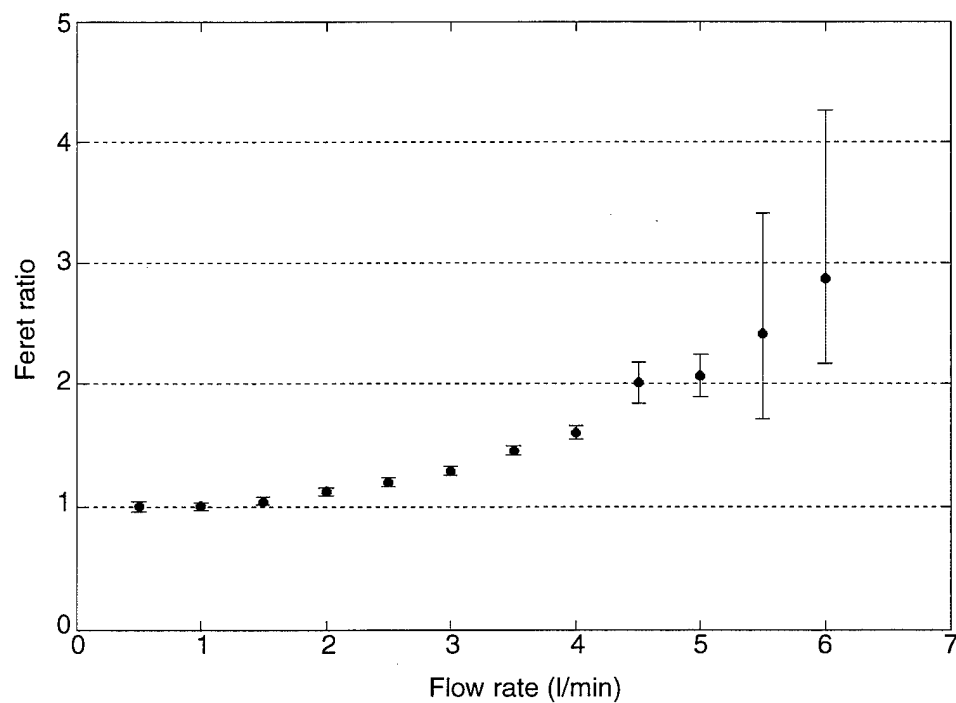Figure 6. Feret ratio plotted as function of flow rate for 20-μm oleic acid droplets.
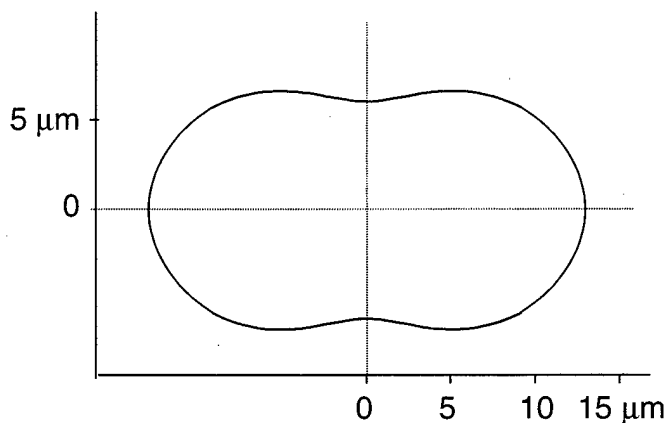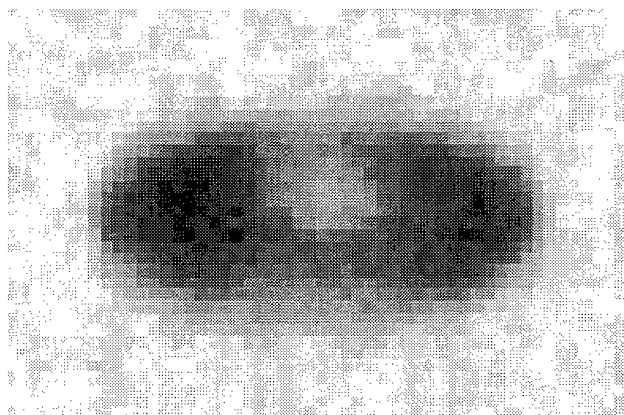

Figure 7. Image of 20-μm nominal diameter oleic acid droplet, together with corresponding computed cross-sectional shape. Computation used density = 0.90 g/cm^3, viscosity = 0.256 Poise, and surface tension = 32 mJ/m^2.

12

5. Droplets with Inclusions

During the process of collecting experimental light-scattering and particle image data of the type described earlier, a phenomenon was observed that has since been attributed to the presence of inclusions in the observed liquid droplets. This is of potential interest, because droplets with internal bodies may occur in environments such as hospital buildings, where entities such as biological organisms can remain viable over long periods by encapsulation within liquids. Similar conditions can apply in the dispersal of biological warfare agents. As a consequence, there is interest in theoretically modeling the light-scattering behavior of such two-component droplets, with the objective of ultimately establishing a means of recognizing their presence in an environment. Reproducible experimental data from droplets with inclusions can thus provide a valuable resource for verifying theoretical inversion methods.

As stated earlier, the VOAG droplets are normally generated into a dry atmosphere, typically <1 %RH. When 20-μm droplets of glycerin, in which water is soluble, were generated into a moist atmosphere at 40 %RH, no perturbations of the expected scattering patterns were observed (see fig. 8a). However, when similar-sized droplets of oleic acid, in which water is insoluble, were generated into the same atmosphere, light-scattering patterns of the type shown in figure 8b were consistently observed. These preliminary scattering data were recorded at a flow rate of 1 l/min.

The striking feature of the oleic acid pattern is the displaced secondary scattering fringes superimposed on the normal concentric rings from a homogeneous sphere. Figure 8c shows a droplet image from the same oleic acid aerosol (although, for the reasons given in sect. 2.2, not from the same droplet as shown in fig. 8b); this image shows the presence of an internal dielectric discontinuity. The positions of the secondary scattering fringes relative to those from the host droplet provide good evidence to support the hypothesis of an inclusion offset vertically upward from the center of the oleic acid host, and, again, this is supported both by the reproducibility of the images of the droplets (such as in fig. 8c) and by theoretical analysis [12]. This upward shift of the inclusion within the host may reasonably be assumed to be due to the density difference between the inclusion and host, as is the case with water and oleic acid (0.998 compared to 0.895 g/cm^3). The higher density water inclusion moves toward the top of the host oleic acid droplet when the droplet is accelerated downward within the airflow through the APS delivery nozzle.

Figure 8. Scattering patterns recorded from droplets generated in 40-%RH environment:
(a) 20-μm-diameter glycerin droplet with no inclusion and
(b) 20-μm oleic acid droplet with inclusion. Image
(c) shows type of droplet giving rise to scattering in image
(b).

(a)

(b)

(c)
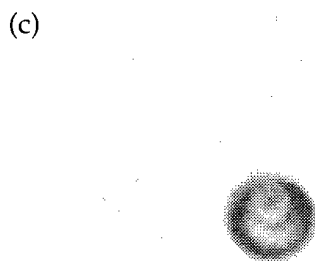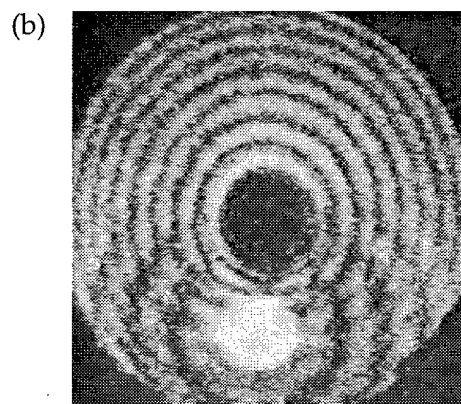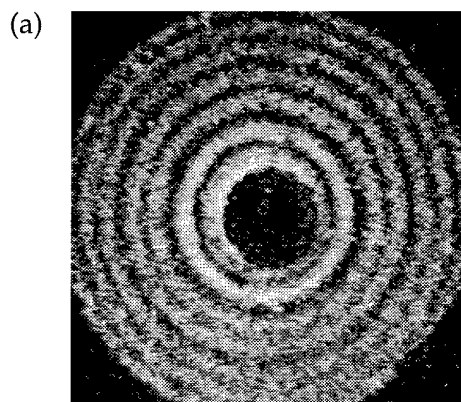
These results are preliminary, and the exact mechanism by which the water inclusion is created is not yet known. One hypothesis is that water vapor condenses onto the original droplets and dissolves into the alcohol present. Once the alcohol has evaporated, the water, which has a higher surface tension than oleic acid, forms a single droplet enveloped by the oleic acid. Thermodynamic modeling of such a system is complex, but has been the subject of recent work by other authors [15,16]. For smaller host droplet sizes, the secondary scattering becomes distorted to yield downward bright arms, as shown in figure 9. Theoretical analysis [12] suggests that this change in scattering is commensurate with an increase in the size of the inclusion relative to the host.

Figure 9. Scattering pattern and image of 16-μm-diameter oleic acid droplet containing inclusion with greater size (relative to host droplet) than that shown in figure 8.
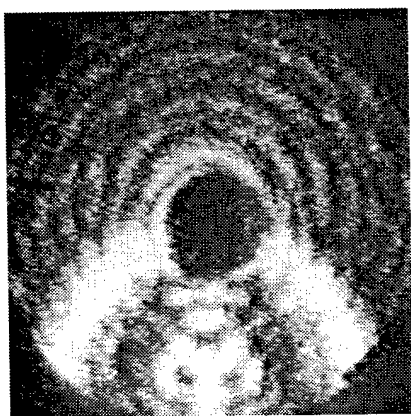
6. Discussion

The experimental data presented in this volume illustrate the complex spatial light-scattering behavior of droplets distorted by accelerating flow fields and droplets containing inclusions. These data are, we believe, the first of their type to be reported. The reproducibility of the experimental data makes them a valuable resource in the development and testing of theoretical inversion models. Such models may ultimately provide a route to the rapid characterization and/or identification of complex droplet morphologies, and this, in turn, could lead to advances in instrumentation for droplet aerodynamic sizing and for the detection of potential bioaerosol hazards in hospital and battlefield situations. In volume 2 of this report, numerically calculated spatial light-scattering data are presented that indicate that theoretical inversion of the light-scattering data is achievable for a variety of droplet morphologies relevant to the experimental conditions described here.

Acknowledgements

References

1. J. K. Agarwal, and R. J. Remiarz, *Development of an Aerodynamic Particle Size Analyser*. National Institute of Occupational Safety and Health, USDHEW-NIOSH contract report 210-80-0800, Cincinnati, OH (1981).

2. P. A. Baron, "Calibration and use of the aerodynamic particle sizer (APS 3300)," *Aerosol Sci. Technol.* **5**, 55–67 (1986).

3. W. D. Griffiths, P. J. Iles, and N. P. Vaughan, "The behaviour of liquid droplets in an APS 3300," *J. Aerosol Sci.* **17**, 427–431 (1986).

4. S. Holler, Y. Pan, R. K. Chang, J. R. Bottiger, S. C. Hill, and D. B. Hillis, "Two-dimensional angular optical scattering for the characterization of airborne microparticles," *Opt. Lett.* **23** (18), 1489–1491 (1998).

5. E. Hirst, P. H. Kaye, and J. R. Guppy, "Light scattering from non-spherical airborne particles: Theoretical and experimental comparisons," *Appl. Opt.* **33** (30), 7180–7187 (1994).

6. P. H. Kaye, K. Alexander-Buckley, E. Hirst, and S. Saunders, "A real-time monitoring system for airborne particle shape and size analysis," *J. Geophys. Res. (Atmospheres)* **101** (D14), 19,215–19,221 (1996).

7. P. H. Kaye, E. Hirst, and Z. Wang-Thomas, "Neural-network based spatial light-scattering instrument for hazardous airborne fiber detection," *Appl. Opt.* **36**, 6149–6156 (1997).

8. K. Willeke and P. A. Baron, *Aerosol Measurement: Principles, Techniques, and Applications*. Van Nostrand Reinhold, New York (1993).

9. W. J. Smith, *Modern Optical Engineering*, McGraw-Hill, New York, pp 439–443 (1966).

10. G. Ananth and J. C. Wilson, "Theoretical analysis of the performance of the TSI Aerodynamic Particle Sizer," *Aerosol Sci. Technol.* **9**, 189–199 (1988).

11. C. F. Bohren and D. R. Huffman, *Absorption & Scattering of Light by Small Particles*. Wiley-InterScience, New York (1983).

12. G. Videen, W. Sun, Q. Fu, D. R. Secker, P. H. Kaye, R. S. Greenaway, E. Hirst, and D. L. Bartley, *Light Scattering From Deformed Droplets and Droplets with Inclusions: Volume 2 Theoretical Results.* U.S. Army Research Laboratory, ARL-TR-2228-II (September 2000).

13. MatLab, "The Mathworks, Inc.," 5.3.0.10183 (R11) ed. (1999).

14. D. L. Bartley, A. B. Martinez, P. A. Baron, D. R. Secker, and E. Hirst, "Droplet distortion in accelerating flow," *J. Aerosol Sci.* (March 2000).

15. T. Vesala, M. Kulmala, R. Rudolf, A. Vrtala, and P. E. Wagner, "Models for condensational growth and evaporation of binary aerosol particles," *J. Aerosol Sci.* **28**, 565–598 (1997).

16. T. Mattila, M. Kulmala, and T. Vesala, "On the condensational growth of a multicomponent droplet," *J. Aerosol Sci.* **28**, 553–564 (1997).

Distribution

Admnstr
Defns Techl Info Ctr
Attn DTIC-OCP
8725 John J Kingman Rd Ste 0944
FT Belvoir VA 22060-6218

DARPA
Attn S Welby
Attn Techl Lib
3701 N Fairfax Dr
Arlington VA 22203-1714

Dir of Defns Rsrch & Engrg
Attn DD TWP
Attn Engrg
The Pentagon
Washington DC 20301

Ofc of the Secy of Defns
Attn ODDRE (R&AT)
The Pentagon
Washington DC 20301-3080

Ofc of the Secy of Defns
Attn OUSD(A&T)/ODDR&E(R) R J Trew
3080 Defense Pentagon
Washington DC 20301-7100

Commanding Officer
Attn NMCB23
6205 Stuart Rd Ste 101
FT Belvoir VA 22060-5275

AMCOM MRDEC
Attn AMSMI-RD W C McCorkle
Redstone Arsenal AL 35898-5240

Dir for MANPRINT
Ofc of the Deputy Chief of Staff for Prsnnl
Attn J Hiller
The Pentagon Rm 2C733
Washington DC 20301-0300

Dir of Chem & Nuc Ops DA DCSOPS
Attn Techl Lib
Washington DC 20301

SMC/CZA
2435 Vela Way Ste 1613
El Segundo CA 90245-5500

TECOM
Attn AMSTE-CL
Aberdeen Proving Ground MD 21005-5057

US Army ARDEC
Attn AMSTA-AR-TD M Fisette
Bldg 1
Picatinny Arsenal NJ 07806-5000

US Army Engrg Div
Attn HNDED FD
PO Box 1500
Huntsville AL 35807

US Army Info Sys Engrg Cmnd
Attn AMSEL-IE-TD F Jenia
FT Huachuca AZ 85613-5300

US Army Natick RDEC Acting Techl Dir
Attn SBCN-T P Brandler
Natick MA 01760-5002

US Army NGIC
Attn Rsrch & Data Branch
220 7th Stret NE
Charlottesville VA 22901-5396

US Army Nuc & Cheml Agency
7150 Heller Loop Ste 101
Springfield VA 22150-3198

US Army Simulation, Train, & Instrmntn
  Cmnd
Attn AMSTI-CG M Macedonia
Attn J Stahl
12350 Research Parkway
Orlando FL 32826-3726

US Army Soldier & Biol Chem Cmnd Dir of
  Rsrch & Techlgy Dirctrt
Attn SMCCR-RS I G Resnick
Aberdeen Proving Ground MD 21010-5423

US Army Strtgc Defns Cmnd
Attn CSSD H MPL Techl Lib
PO Box 1500
Huntsville AL 35807

Distribution (cont'd)

US Army Tank-Automtv Cmnd Rsrch, Dev, &
  Engrg Ctr
Attn AMSTA-TR J Chapin
Warren MI 48397-5000

US Army Train & Doctrine Cmnd
Battle Lab Integration & Techl Dirctrt
Attn ATCD-B
FT Monroe VA 23651-5850

US Military Academy
Mathematical Sci Ctr of Excellence
Attn MADN-MATH MAJ M Huber
Thayer Hall
West Point NY 10996-1786

Chief of Nav OPS Dept of the Navy
Attn OP 03EG
Washington DC 20350

Nav Surface Warfare Ctr
Attn Code B07 J Pennella
17320 Dahlgren Rd Bldg 1470 Rm 1101
Dahlgren VA 22448-5100

US Dept of Energy
Attn Techl Lib
Washington DC 20585

Central Intllgnc Agency
Dir DB Standard
Attn OSS/KPG/DHRT
1E61 OHB
Washington DC 20505

Hicks & Associates Inc
Attn G Singley III
1710 Goodrich Dr Ste 1300
McLean VA 22102

US Army Rsrch Ofc
Attn AMSRL-RO-D JCI Chang
Attn AMSRL-RO-EN W D Bach
Attn AMSRL-RO
PO Box 12211
Research Triangle Park NC 27709

US Army Rsrch Lab
Attn AMSRL-CI-AI-R Mail & Records Mgmt
Attn AMSRL-CI-AP Techl Pub (3 copies)
Attn AMSRL-CI-LL Techl Lib (3 copies)
Attn AMSRL-DD J M Miller
Attn AMSRL-IS-EE G Videen (10 copies)
Adelphi MD 20783-1197

REPORT DOCUMENTATION PAGE

Public reporting burden for this collection of information is estimated to average 1 hour per response, including the time for reviewing instructions, searching existing data sources, gathering and maintaining the data needed, and completing and reviewing the collection of information. Send comments regarding this burden estimate or any other aspect of this collection of information, including suggestions for reducing this burden, to Washington Headquarters Services, Directorate for Information Operations and Reports, 1215 Jefferson Davis Highway, Suite 1204, Arlington, VA 22202-4302, and to the Office of Management and Budget, Paperwork Reduction Project (0704-0188), Washington, DC 20503.

1. AGENCY USE ONLY *(Leave blank)*	2. REPORT DATE September 2000	3. REPORT TYPE AND DATES COVERED Final, FY99

4. TITLE AND SUBTITLE Light Scattering from Deformed Droplets and Droplets with Inclusions:
Volume I. Experimental Results

5. FUNDING NUMBERS

DA PR: N/A

PE: 61102A

6. AUTHOR(S) David R. Secker, Richard Greenaway, Paul H. Kaye, Edwin Hirst (University of Hertfordshire, Hatfield, UK), David Bartley (National Institute for Occupational Safety and Health, Cincinnati, OH), Gorden Videen (ARL)

7. PERFORMING ORGANIZATION NAME(S) AND ADDRESS(ES)
U.S. Army Research Laboratory
Attn: AMSRL-CI-EM   email: gvideen@arl.army.mil
2800 Powder Mill Road
Adelphi, MD 20783-1197

8. PERFORMING ORGANIZATION REPORT NUMBER
ARL-TR-2228-I

9. SPONSORING/MONITORING AGENCY NAME(S) AND ADDRESS(ES)
U.S. Army Research Laboratory
2800 Powder Mill Road
Adelphi, MD 20783-1197

10. SPONSORING/MONITORING AGENCY REPORT NUMBER

11. SUPPLEMENTARY NOTES
ARL PR: 7FEJ70
AMS code: 61110253A11

12a. DISTRIBUTION/AVAILABILITY STATEMENT Approved for public release; distribution unlimited.

12b. DISTRIBUTION CODE

13. ABSTRACT *(Maximum 200 words)*

This is the first of two volumes dealing with experimental and theoretical results from the scattering of light by deformed liquid droplets and droplets with inclusions. Characterizing droplet deformation could lead to improved measurement of droplet size by commercial aerodynamic particle sizing instruments. Characterizing droplets with inclusions can be important in some industrial, occupational, and military monitoring scenarios. The nozzle assembly from a TSI aerodynamic particle sizer was used to provide the accelerating flow conditions in which experimental data were recorded. A helium-neon (HeNe) laser was employed to generate the light-scattering data, and an externally triggered, pulsed copper vapor laser provided illumination for a droplet imaging system, arranged orthogonal to the HeNe scattering axis. The observed droplet deformation correlates well over a limited acceleration range, with theoretical predictions derived from analytical solution of the Navier-Stokes equation.

14. SUBJECT TERMS Scattering, aerosols			15. NUMBER OF PAGES 27
			16. PRICE CODE

17. SECURITY CLASSIFICATION OF REPORT Unclassified	18. SECURITY CLASSIFICATION OF THIS PAGE Unclassified	19. SECURITY CLASSIFICATION OF ABSTRACT Unclassified	20. LIMITATION OF ABSTRACT UL